

Reprogramming the Tumor Immune Microenvironment Through Activatable Photothermal Therapy and GSH depletion Using Liposomal Gold Nanocages to Potentiate Anti-Metastatic Immunotherapy

Jiayi Li, Kaifan Zheng, Luping Lin, Mengdi Zhang, Ziqi Zhang, Junyu Chen, Shaoguang Li, Hong Yao, Ailin Liu, Xinhua Lin,* Gang Liu,* and Bing Chen*

Cancer immunotherapy offers significant clinical benefits for patients with advanced or metastatic tumors. However, immunotherapeutic efficacy is often hindered by the tumor microenvironment's high redox levels, leading to variable patient outcomes. Herein, a therapeutic liposomal gold nanocage (MGL) is innovatively developed based on photo-triggered hyperthermia and a releasable strategy by combining a glutathione (GSH) depletion to remodel the tumor immune microenvironment, fostering a more robust anti-tumor immune response. MGL comprises a thermosensitive liposome shell and a gold nanocage core loaded with maleimide. The flexible shell promotes efficient uptake by cancer cells, enabling targeted destruction through photothermal therapy while triggering immunogenic cell death and the maturation of antigen-presenting cells. The photoactivated release of maleimide depletes intracellular GSH, increasing tumor cell sensitivity to oxidative stress and thermal damage. Conversely, GSH reduction also diminishes immunosuppressive cell activity, enhances antigen presentation, and activates T cells. Moreover, photothermal immunotherapy decreases elevated levels of heat shock proteins in tumor cells, further increasing their sensitivity to hyperthermia. In summary, MGL elicited a robust systemic antitumor immune response through GSH depletion, facilitating an effective photothermal immunotherapeutic strategy that reprograms the tumor microenvironment and significantly inhibits primary and metastatic tumors. This approach demonstrates considerable translational potential and clinical applicability.

risk of recurrence underscores the necessity for continued research and personalized therapeutic approaches to enhance patient outcomes.^[1] Cancer immunotherapy, which leverages the immune system of the body to identify and eliminate cancer cells, offers patients the potential for durable remission and even complete eradication of the disease.^[2] The advent of immunotherapy has revolutionized the cancer treatment landscape, offering new hope for patients with challenging malignancies.^[3] The tumor microenvironment (TME) is crucial to the effectiveness of cancer immunotherapy, which is a complex ecosystem comprising various cellular and noncellular components, including tumor cells, immune cells, blood vessels, fibroblasts, extracellular matrix components, and biochemical factors.^[4] The intricate interactions among these components of TME profoundly influence tumor behavior and immune responses. Understanding these interactions is essential for enhancing immunotherapeutic outcomes.


High redox levels within the TME can enhance genetic instability, angiogenesis, invasion, and metastasis, significantly

influencing tumor progression, therapy resistance, and immune evasion.^[5] Glutathione (GSH)—a crucial antioxidant component found primarily within cells—plays a key role in protecting cells from oxidative stress, detoxification, and immune

1. Introduction

Surgery, radiotherapy, and chemotherapy remain the current standard treatments in the battle against cancer. However, the

J. Li, K. Zheng, L. Lin, M. Zhang, Z. Zhang, J. Chen, S. Li, H. Yao, A. Liu, X. Lin, B. Chen
Key Laboratory of Nanomedical Technology (Education Department of Fujian Province)
Department of Pharmaceutical Analysis
School of Pharmacy
Fujian Medical University
Fuzhou, Fujian 350122, P. R. China
E-mail: 13906909638@163.com; BingChen_001@fjmu.edu.cn

 The ORCID identification number(s) for the author(s) of this article can be found under <https://doi.org/10.1002/sml.202407388>

DOI: 10.1002/sml.202407388

G. Liu
State Key Laboratory of Molecular Vaccinology and Molecular Diagnostics & Center for Molecular Imaging and Translational Medicine
School of Public Health
Xiamen University
Xiamen 361102, China
E-mail: gangliu.cmitm@xmu.edu.cn

response, among others.^[6] Many tumor types exhibit a unique microenvironment characterized by overexpressed GSH levels (≈ 10 mM), which results in resistance against chemotherapy and radiotherapy, as well as the development of an immunosuppressive TME.^[7] High GSH levels can impair the ability of antigen-presenting cells (APCs) to effectively present tumor antigens to T cells and produce cytokines, resulting in suboptimal T cell activation and diminished tumor immune recognition.^[8] Additionally, elevated GSH levels can enhance the survival of myeloid-derived suppressor cells and regulatory T cells (T_{regs}), which inhibit the activation and proliferation of effector T cells, thereby facilitating immune surveillance evasion. In summary, elevated GSH levels in tumor cells and the TME pose significant obstacles to effective cancer treatment. GSH-depleting agents offer direct benefits for oxidative therapy and enhance antitumor immune responses by promoting immunogenic cell death effect and dendritic cell (DC) maturation.^[9] Therefore, efficiently targeting the TME and intracellular GSH is a promising strategy for enhancing robust antitumor immune responses and clinical cancer treatment.^[10] To date, several GSH-depleting drugs, such as auromain, diethylmaleate, L-buthionine sulfoximine (BSO), and phenethyl isothiocyanate (PEITC), have been utilized in cancer treatment.^[11] However, clinical studies indicate that monotherapy focusing on depleting intracellular GSH offers limited overall survival benefits. Conversely, combining GSH depletion with other therapeutic approaches can significantly enhance treatment sensitivity and reduce potential resistance.^[12]

Photothermal therapy (PTT) has become increasingly popular in antitumor treatment owing to its advantages, such as precise site control, high killing efficiency, and minimal side effects.^[13] The photonic hyperthermia effect can trigger cell death and release tumor antigens, which enhances cancer cell visibility to the immune system.^[14] However, PTT alone is insufficient to effectively trigger an antitumor immune response owing to the dual limitations of the immunosuppressive TME and the elevated expression of heat shock proteins (HSPs).^[15] Combining PTT with strategies for GSH depletion can effectively remodel the tumor immune microenvironment, promoting a more robust antitumor immune response.^[16] This combined approach has the potential to enhance the overall efficacy of cancer immunotherapy and improve patient treatment outcomes. Therefore, leveraging GSH-depleting antitumor strategies to leverage the immunogenic cell death effect of PTT and serve as adjuvants for enhancing immune responsiveness is crucial. Thiols—the key active sites of GSH—are essential for their antioxidant properties, and blockage of thiols can undermine their antioxidant effects.^[17] Recent studies show that active compounds containing the maleimide (MAL) group can irreversibly react with thiols via Michael addition and have the potential to be developed as superior adjuvant candidates in combination with strategies aimed at achieving an effective systemic tumor immune response.^[18]

Gold nanocages (GNCs) are exceptional candidate platforms for various biomedical applications owing to their distinctive properties, such as hollow interiors, porous walls, specific near-infrared region absorption, high photothermal conversion efficiency, modifiability, and biocompatibility.^[19] GNCs have been optimized for large-scale production while maintaining their quality, such as monodisperse size, adjustable optical characteristics and stability, and a high surface-area-to-volume ratio.

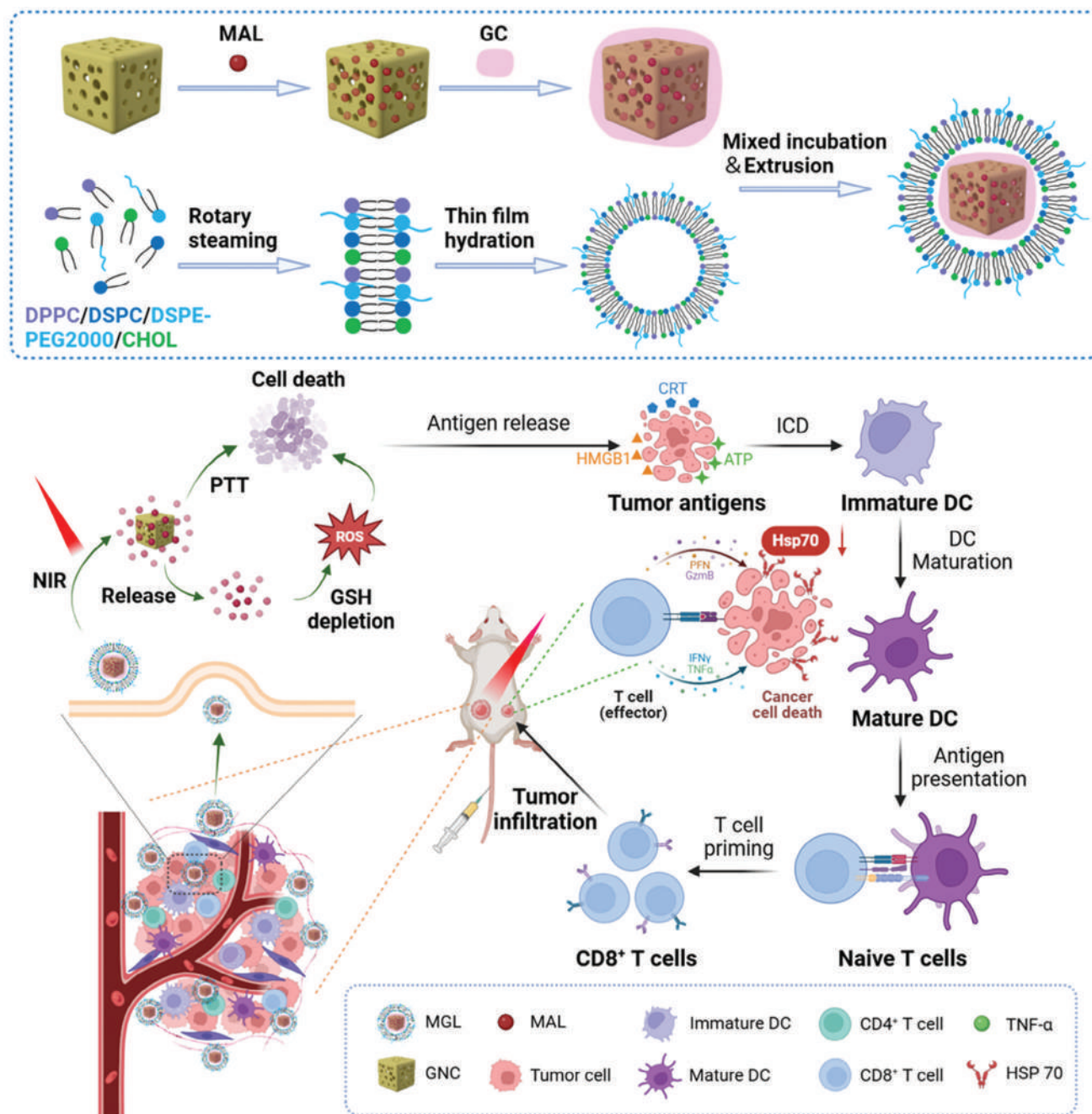
These features make GNCs suitably useful for applications such as drug delivery, imaging, and therapeutics.^[20] To date, numerous gold formulations have been explored for various clinical and preclinical applications, with some receiving FDA approval for anti-inflammatory and anti-arthritis purposes.^[21] Clinical applications of these gold formulations have demonstrated promising properties for immune system modulation and anti-inflammatory effects.^[22] However, the hollow structure of GNCs may result in potential drug leakage and insufficient stability as a drug delivery vehicle. To overcome this challenge, liposomes, which mimic biological membranes, are utilized to enhance stability, extend circulation time, and enable controlled drug release.^[23]

Therefore, this study aims to develop a photo-triggered liposomal gold nanocarriers based on GNC for precise and synergistic photothermal immunotherapy. **Scheme 1** shows that GNC serves as a drug delivery vehicle, loaded with immune adjuvant—MAL and finally coated with heat-sensitive liposomes (resulting in MAL@GNC coated with heat-sensitive liposomes, MGL). MAL not only depletes GSH, resulting in up regulated reactive oxygen species (ROS) levels and tumor cell apoptosis, but also promotes the release of subsequent damage-associated molecular patterns (DAMPs). These DAMPs further enhanced antigen presentation facilitated DC maturation, and increased cytotoxic T cells ($CD8^+$ T cells) infiltration, thereby enhancing antitumor immune response. Moreover, combining photo-triggered hyperthermia with a GSH-depleting drug can upregulate ROS levels in tumor cells and DCs, thereby enhancing the photothermally induced immunogenic cell death (ICD) effect. This approach reduces immunosuppression, further promoting DC maturation and antigen presentation and activating $CD8^+$ T cells to recognize and kill tumor cells. Simultaneously, the cytokine $TNF-\alpha$ secreted by activated T cells can downregulate HSP 70 expression in tumor cells, enhancing their sensitivity photothermally.^[24] This enhanced the effectiveness of PTT and successfully achieved the synergistic therapy of light, heat, and immunity. Overall, this innovative synergistic therapy—combining photo-triggered hyperthermia with GSH depletion and immune modulation—holds promise for providing long-term, durable remission, enhancing cancer treatment effectiveness/therapeutic efficacy, and restraining metastasis.

2. Results and Discussion

2.1. Preparation and Characterization of MGL

The MGL was fabricated using a previously established method with slight modifications.^[25] First, silver cubes (AgNCs) with a maximum UV absorption wavelength of 424 nm were prepared using a polyalcohol reduction method (Figure S1A, Supporting Information). The silver cube was then converted into a GNC through an electric displacement reaction, which was halted when the maximum absorption peak reached 808 nm (Figure S1B, Supporting Information). Moreover, the gold and silver contents in the GNCs were quantified using ICP-OES. The results showed concentrations of $C_{\text{Au}} = 46.32 \mu\text{g mL}^{-1}$ and $C_{\text{Ag}} = 21.44 \mu\text{g mL}^{-1}$ in the GNC solution, with an absorbance of $A_{800 \text{ nm}} = 1.741$. Second, the GNCs were loaded with the GSH-depleting adjuvant MAL and coated with heat-sensitive



Scheme 1. Schematic illustration of photo-triggered hyperthermia and GSH depletion drug release for enhanced photothermal immunotherapy. The enhanced synergistic effect of photothermal immunotherapy relies on the remodeled tumor immunosuppressive microenvironment and alleviated HSPs owing to precise in situ excellent hyperthermia therapy and MAL adjuvant release.

liposomes using a film dispersion and extrusion method to form the MGL.^[26]

Figure 1A,B shows that the dynamic light scattering (DLS) analysis confirmed that MGL exhibited a well-defined monodispersed distribution with a 65.58 nm average size, which was larger than those of GNC and AgNCs. For a more precise observation, transmission electron microscopy was used to characterize the nanostructure of MGL, revealing that a membranous liposome layer successfully encapsulated the MAL-loaded GNCs.

Furthermore, the zeta potential measurements of AgNCs, GNC, GNC@GC, and MGL showed consistent characteristics associated with the liposomal shell, confirming that MGL was successfully fabricated (Figure 1C). Additionally, the maximum UV absorption peak of MGL was ≈ 800 nm, which was similar to that of GNC, indicating that the liposome encapsulation did not affect the UV absorption properties of the GNC (Figure 1D).

To further evaluate the drug-loading capacity and quality of MGL, high-performance liquid chromatography (HPLC) and a

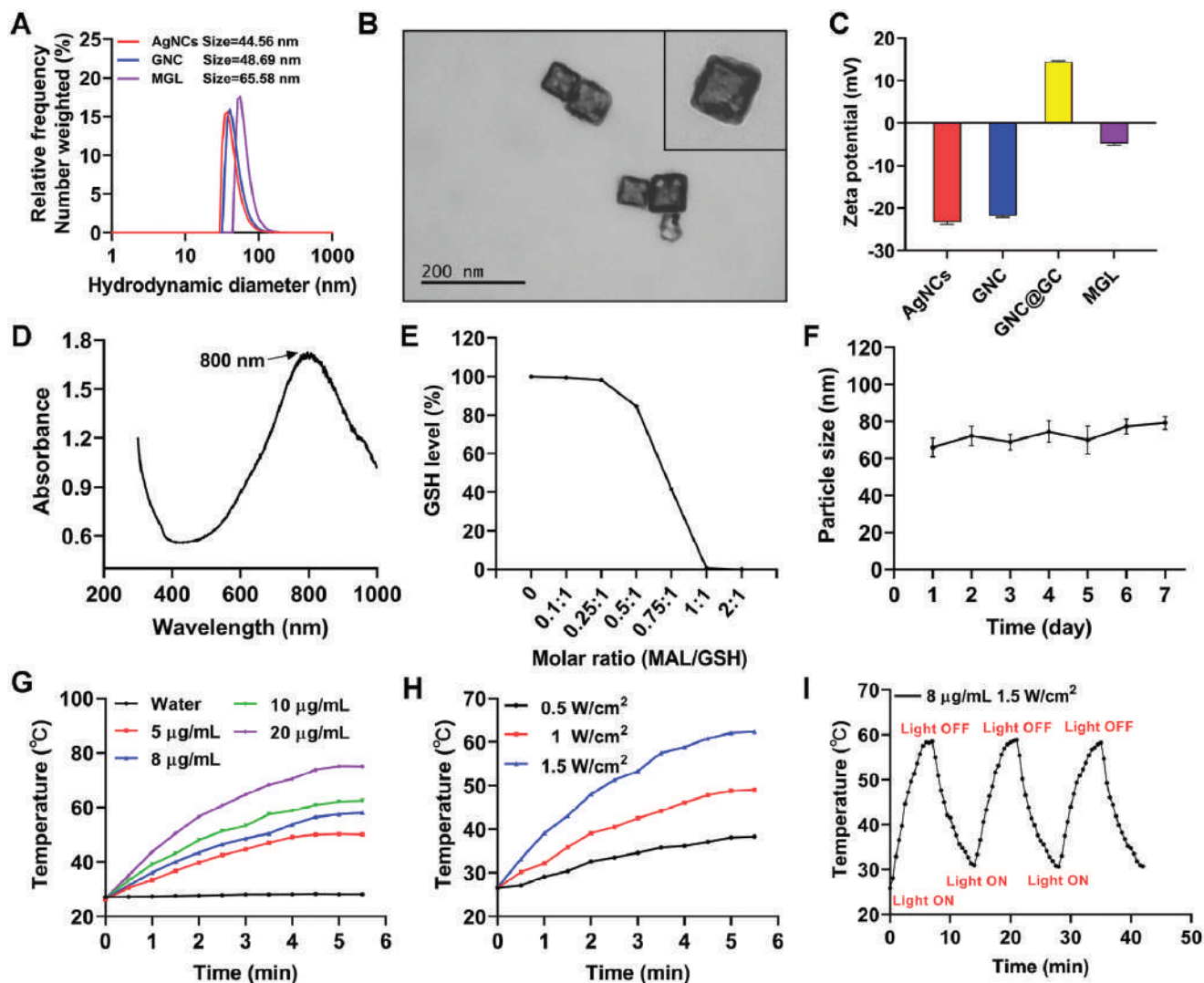


Figure 1. Preparation and characterization of MAL. A) Size distribution of AgNCs, GNC, and MAL. B) The transmission electron microscopy (TEM) images of MGL (Scale bar: 200 nm). C) zeta potential diagram of AgNCs, GNC, GNC@GC, and MAL. D) The UV-vis spectra of MGL. E) The relative GSH level after treatment with increasing molar ratios of MAL/GSH ($n = 3$). F) The stability test of MGL ($n = 3$). G) Temperature-changing curve of MGL suspension ($C_{MGL} = 0, 5, 8, 10,$ and $20 \mu\text{g mL}^{-1}$) was exposed to an 808 nm laser (1.5 W cm^{-2} for 5 min) and the temperature was monitored at 30 s intervals for 5 min. H) Temperature-changing curve of MGL suspension ($C_{MGL} = 10 \mu\text{g mL}^{-1}$) was exposed to 0.5, 1, and 1.5 W cm^{-2} irradiation intensity. I) Assessment of the photothermal stability of MGL under 808 nm laser irradiation (1.5 W cm^{-2} for 5 min) through three cycles of laser on/off.

particle size analyzer were employed to evaluate its drug-loading efficiency and stability. The MAL loading content of MGL was determined to be $1.41 \pm 0.05\%$. Moreover, DLS was utilized to investigate the thermal stability of MGL for 7 days at room temperature. The results showed that MGL maintained a stable particle size of $\approx 65 \text{ nm}$, without aggregation or sedimentation, suggesting that the nanoparticles exhibited good stability and resistance to degradation under physiological conditions (Figure 1F).

2.2. MAL-Mediated Glutathione Depletion

Overexpression of GSH in the TME and tumor cells reduced the efficacy of ROS-based therapies, including chemotherapy and

radiotherapy.^[27] Additionally, this overexpression may promote the formation of an immunosuppressive microenvironment and inhibit the antitumor lymphocyte activity. MAL could react with thiols through Michael's addition, forming covalent bonds under physiological or weakly acidic conditions within the TME. This reaction effectively depletes excess GSH, resulting in its inactivation.^[28] MAL can interfere with GSH synthesis, eliminating antioxidant protective effects, disrupting the high redox level of the TME, and enhancing the therapeutic sensitivity of tumor cells in a dose-dependent manner. At a MAL/GSH molar ratio of $<0.25:1$, only a small amount of GSH was consumed, but as the proportion of MAL increased, GSH levels declined rapidly. When the molar ratio reached $1:1$, GSH was almost entirely depleted in pH 7.4 (Figure 1E). These findings indicate that MAL-mediated GSH depletion is an irreversible process characterized

by rapid reaction and strong consumption capacity, making MAL a promising candidate for GSH blockade.

2.3. Photothermal Properties of MGL

Our previous research has shown that GNCs exhibit a strong surface plasmon resonance absorption peak at ≈ 808 nm, demonstrating their exceptional photothermal conversion efficiency.^[25,29] Figure 1G,H shows the temperature change in MGL was positively correlated with its concentration and laser irradiation power. When MGL suspensions ($C_{\text{MGL}} = 0, 5, 8, 10,$ and $20 \mu\text{g mL}^{-1}$) were subjected to 1.5 W cm^{-2} laser irradiation, the temperature increased rapidly during the irradiation initial phase, reaching a plateau after ≈ 5 min. Furthermore, when an MGL suspension ($C_{\text{MGL}} = 10 \mu\text{g mL}^{-1}$) was subjected to varying laser irradiation intensities, the temperature increased sequentially within the range of $0.5\text{--}1.5 \text{ W cm}^{-2}$ irradiation intensity. When $8 \mu\text{g mL}^{-1}$ of MGL was subjected to an 808 nm laser irradiation at 1.5 W cm^{-2} for 5 min, the temperature rapidly rose to ≈ 60 °C, further confirming its exceptional photothermal conversion efficiency. Moreover, the temperature variation trend observed in the GNC solution was approximately comparable to that of MGL (Figure S2, Supporting Information), indicating that neither the liposome encapsulation nor MAL loading compromised the photothermal conversion performance of the GNC. The photothermal stability of the MGL was further assessed. Across the three light exposure cycles, the temperature increase remained consistent (Figure 1I). This consistent performance indicates good photothermal stability of the material. These findings confirm that the synthesized MGL nanoparticles exhibit exceptional photothermal conversion efficiency and good photothermal stability.

2.4. Cellular Internalization and Intracellular GSH Detection

To assess the cellular uptake behavior of MGL, the fluorescence intensity of intracellular fluorescein isothiocyanate (FITC)-labeled MGL was investigated in the EMT-6 and 4T1 cells over an extended culture time. Figures 2A and S3 (Supporting Information) show that a time-dependent intracellular FITC-labeled MGL was observed using a confocal laser scanning microscope (CLSM), and the results showed that the green fluorescence signal gradually increased with increasing incubation time. Furthermore, the cellular internalization of MGL was further quantitatively verified by flow cytometry. Quantitative analysis using flow cytometry further confirmed the cellular internalization of MGL. The results showed a significant FITC signal in EMT-6 and 4T1 cells treated with FITC-labeled MGL after 4 h of incubation, which is consistent with the CLSM results (Figure 2B,C; S4, Supporting Information). These findings confirm that the cellular membrane surface of MGL is readily internalized and accumulated within tumor cells.

Subsequently, we further investigated the MAL dynamic release process of MAL after cellular uptake of MGL, as well as the intracellular GSH consumption and ROS upregulation in EMT-6 and 4T1 cells after various treatments. To assess intracellular GSH levels after various treatments, the ThiolTracker

Violet fluorescent dye was employed to evaluate whether MAL could effectively deplete the GSH levels by reacting with mercaptan. Figure 2E and Figure S5 (Supporting Information) show that the intracellular GSH levels in EMT-6 and 4T1 cells gradually decreased, whereas no significant change was observed in the control group (PBS group). MAL effectively reduced the GSH levels in 4T1 and EMT-6 cells to 29.9% and 57.1% , respectively. However, the MGL treatment group led to reductions of 45.4% and 65.8% in the same cell lines. This may be attributed to the slow-release characteristics of MGL coated with liposomes, which may result in incomplete drug release. Consequently, their GSH levels remained slightly higher than those of the free MAL-treated group. These findings suggest that MAL can effectively deplete GSH levels within breast cancer cells.

Following effective GSH depletion by MAL or MGL, the intracellular redox balance was disrupted, leading to increased intracellular ROS levels, which induced tumor cell cytotoxicity or enhanced their therapeutic sensitivity. Therefore, the DCFH-DA probe was used to determine intracellular ROS levels. The observed trends in intracellular ROS levels were consistent in the two strains after treatment in different groups. The MAL-treated group exhibited the highest green fluorescence intensity, followed by the MGL-treated group (Figure 2D; Figure S6, Supporting Information), indicating that MAL can significantly increase intracellular ROS levels by consuming GSH.

2.5. Cytotoxicity Analysis and Migration Inhibition of MGL

The cytotoxicities of GNC, MAL, and MGL with or without irradiation were assessed in 4T1 and EMT-6 cells using the MTT assay. Figure 2F and Figure S7 (Supporting Information) show that the GNC group maintained a higher survival rate even at elevated concentrations, demonstrating its excellent biocompatibility. However, upon NIR laser irradiation, cell viability showed a dose-dependent relationship with its concentration, suggesting that GNC-based photothermal therapy can effectively induce tumor cell death. The cytotoxicity of MAL exhibited a significant dose-dependency, with IC_{50} values of $5.50 \mu\text{g mL}^{-1}$ in 4T1 and $7.73 \mu\text{g mL}^{-1}$ in EMT-6 cells, primarily owing to increased ROS levels following GSH depletion. The cytotoxicity of MGL was slightly lower than that of MAL at the same concentration, which may be attributed to MGL surface liposome encapsulation, preventing the complete release of MAL. However, in the MGL+NIR group, laser irradiation significantly enhanced cytotoxicity, resulting in IC_{50} values of 2.82 and $3.84 \mu\text{g mL}^{-1}$, respectively, which were much lower than those observed in the other groups.

Increased ROS levels in tumor cells can result in oxidative stress and trigger apoptosis. To further investigate the effects of various treatments on apoptosis, we employed the Annexin V-FITC/propidium iodide assay, followed by flow cytometry analysis. Figures 3A and S8 (Supporting Information) show that the overall apoptosis rate in the 4T1 and EMT-6 cell lines treated with MGL or GNC combined with irradiation was significantly higher than that of the other groups. This showed the potent synergistic therapeutic effect of hyperthermia combination therapy. The MGL group exhibited the highest apoptosis rates after irradiation,

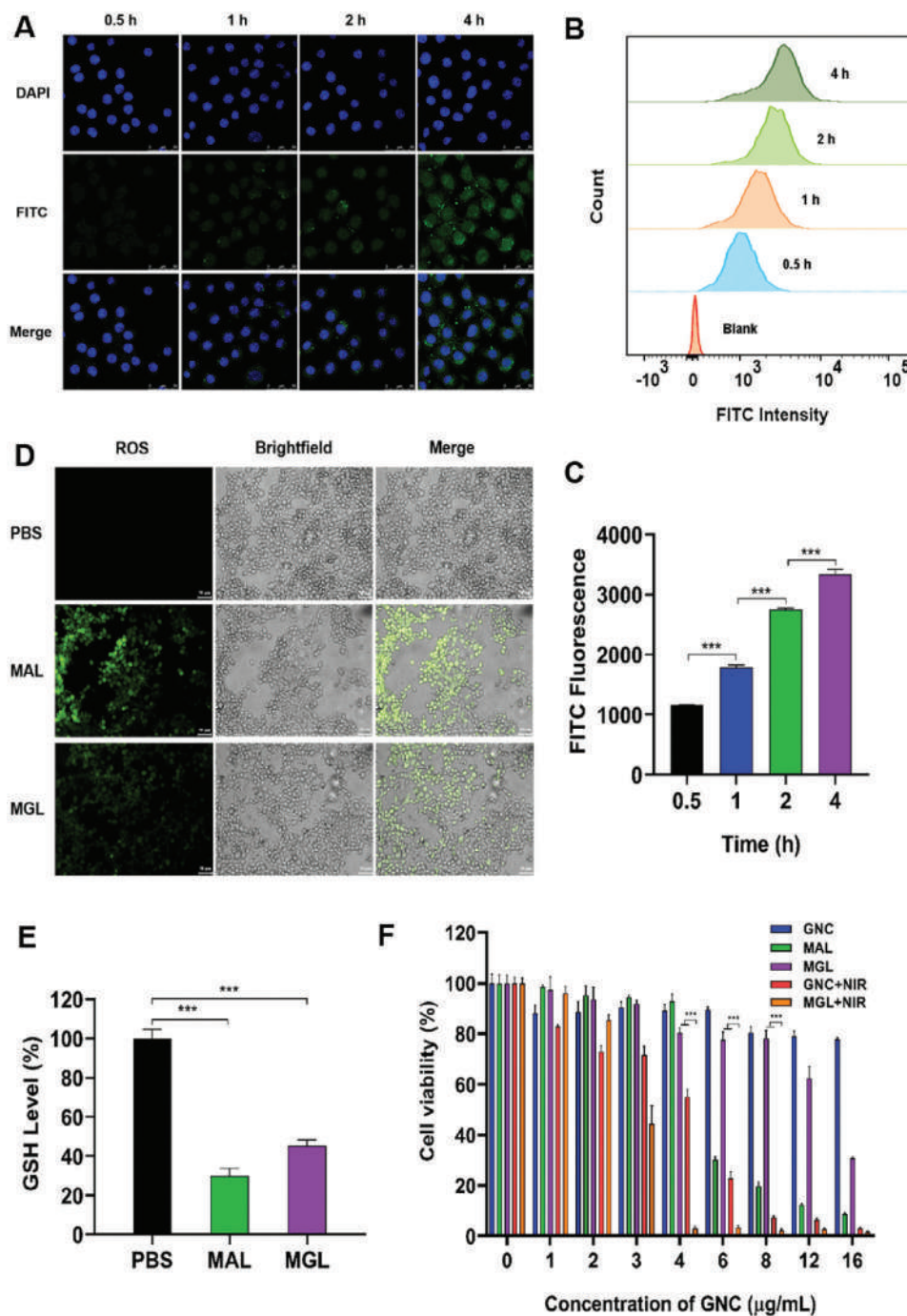


Figure 2. Cellular uptake and cytotoxicity of MGL in 4T1 cells. A) Confocal microscopy images of intracellular uptake of MGL from 4T1 cell cultures treated with MGL for 0.5, 1, 2, and 4 h. (Blue, nuclei; green, MGL. Scale bar: 25 μm). B) Flow cytometry analysis and C) statistical analysis of intracellular uptake of 4T1 cells after incubation with MGL for 0.5, 1, 2, and 4 h. D) Fluorescence images of intracellular ROS levels in 4T1 cells after treatment with PBS, MAL, and MGL (Scale bars, 50 μm). E) Intracellular GSH level detection in 4T1 cells after treatment with PBS, MAL, and MGL in pH 7.4. F) Evaluation of cytotoxic effects of various concentrations of GNC, MAL, and MGL with/without irradiation on 4T1 cells for 24 h, with cell viability determined using the MTT assay. Data are presented as mean ± SD (*n* = 5).

reaching 85.2% and 97.2% in 4T1 and EMT-6 cells, respectively. Furthermore, the MAL group showed a slightly higher apoptosis rate than that in the MGL group, which was attributed to the ability of MAL to deplete GSH. Conversely, the GNC group exhibited apoptosis rates similar to those in the control group,

which were consistent with the results of the MTT assay. In summary, these findings demonstrate that photothermal therapy is highly effective in killing tumor cells, and the synergistic MAL-induced ROS oxidative stress could further enhance tumor cell apoptosis.

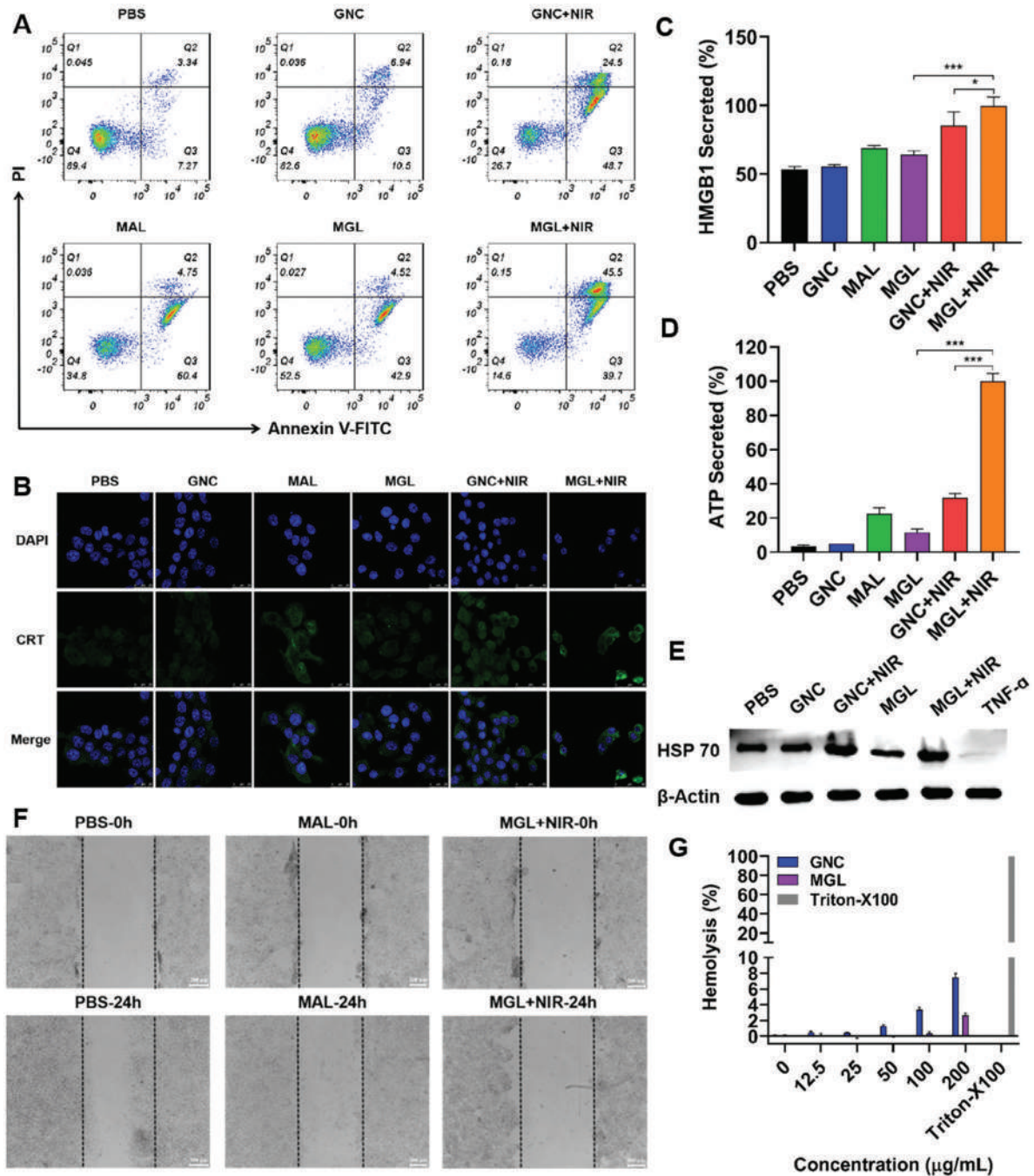


Figure 3. Cellular mechanism action study of MAL and MGL. A) Flow cytometry analysis of cell apoptosis after treatment with PBS, GNC, GNC + NIR, MAL, MGL, and MGL + NIR. B) Confocal microscopy images of calreticulin (CRT) expression after treatment with PBS, GNC, GNC + NIR, MAL, MGL, and MGL + NIR. C) ELISA was used to analyze the HMGB1 secretion and D) ATP release after treatment with PBS, GNC, GNC + NIR, MAL, MGL, and MGL + NIR. E) Western blot assay examining the HSP 70 expression after treatment with PBS, GNC, GNC + NIR, MGL, MGL + NIR, and TNF- α . F) Cell migration levels after 24 h treatment of 4T1 cells with different materials (Scale bar: 200 μ m). G) Evaluation of plasma compatibility between GNC and MGL at different concentrations. Data are displayed as mean \pm SD ($n = 3$), * $p < 0.05$, ** $p < 0.01$, and *** $p < 0.001$.

The migration of tumor cells was further assessed in the EMT-6 and 4T1 cells, as shown in Figure 3F and Figures S9–S10 (Supporting Information). After 24 h, the GNC and control (PBS) groups exhibited the highest levels of cell migration. Conversely, MAL, MGL, and GNC with irradiation groups could effectively in-

hibit tumor cell migration, although some migration persisted, whereas the MGL with irradiation group displayed the most pronounced inhibitory effect, with no observable cell migration. These findings suggest that the synergistic therapy can further inhibit tumor cell proliferation and reduce their repair capabilities.

2.6. Immunogenic Cell Death-Inducing Capability

Localized hyperthermia combined with ROS-based therapies can effectively induce immunogenic cell death by promoting the release of DAMPs. These therapies facilitate the maturation and activation of APC and drive the release of cytokines that modulate immune responses.^[30] This cascade of events is crucial for activating the immune system, thereby enhancing the ability of the body to recognize and eliminate tumor cells. Therefore, the synergistic therapeutic effects of ICD induced in vitro were further studied. The results showed the changing trend of DAMPs released by 4T1 and EMT-6 cells. These DAMPs primarily include calreticulin (CRT) exposure, high-mobility group protein B1 (HMGB1), and ATP release.

4T1 cells were treated with PBS, GNC, MAL, MGL, GNC with irradiation, and MGL with irradiation groups, respectively, and stained with CRT-APC antibody and DAPI, and then the expression of CRT was observed by confocal laser scanning microscope (CLSM) (Figure 3B). The results showed no CRT exposure in the PBS and GNC groups. However, a pronounced green fluorescence was observed following laser irradiation, indicating that PTT-induced CRT exposure. Additionally, MAL-induced ROS oxidative stress effectively enhanced CRT exposure, with fluorescence intensity slightly higher than that observed in the MGL group. This suggests that the increased ROS levels induced by GSH depletion enhanced the tumor cell-killing effect. The MGL with irradiation group exhibited the highest green fluorescence, much higher than that observed in the other groups. This indicates that the synergistic effect of PTT and ROS further enhances the ICD effect.

HMGB1 release and ATP secretion were quantified using ELISA and ATP assay kits, respectively. Figure 3C,D shows the results, and the trend of the change was consistent with that of CRT exposure. The MGL with irradiation group showed the highest levels of HMGB1 and ATP secretion, confirming the enhanced efficacy of the combined treatment group (Figures S11–S13, Supporting Information). Both CRT and HMGB1 can enhance the maturation and activation of dendritic cells, which are essential for initiating adaptive immune responses. The release of ATP can lead to the activation of T cells, particularly through the engagement of purinergic receptors, enhancing their proliferation and cytotoxic activity against tumor cells.^[31] These findings further confirm that PTT can successfully induce the ICD effect. Additionally, this synergistic MAL-induced ROS oxidative stress can further enhance the ICD effect, offering a foundation for a series of antitumor immune responses.

2.7. MGL Reprograms the Tumor Microenvironment and Inhibits Heat Shock Protein Expression

While single hyperthermia- and ROS-based therapies can effectively suppress tumors during their early stages, the subsequent reduction in tumor sensitivity is primarily because of the activation of self-protective mechanisms in tumor cells. The upregulation of intracellular HSP levels not only aids in enhancing treatment resistance but also contributes to tumor immune evasion, promotes angiogenesis, and facilitates metastasis.^[32] MGL combined with a synergistic strategy of GSH depletion and pho-

tothermal immunotherapy could effectively induce the ICD effect and activate the host immune response. This activation mobilizes antitumor lymphocytes and promotes the secretion of cytokines such as TNF- α , which can inhibit HSP expression in tumor cells.^[33] Changes in HSP 70 expression, following various treatments, were examined to assess whether MGL could downregulate HSP expression and thereby enhance the synergistic therapeutic effect. Figure 3E shows that HSP 70 expression was significantly upregulated in the GNC and MGL groups after laser irradiation compared to that in the control group. However, HSP 70 expression in the MGL group treated with irradiation and TNF- α was significantly reduced, even lower than that in the control group. These findings suggest that the enhanced antitumor immune response, driven by synergistic therapy, can successfully regulate HSP 70 expression, thereby enhancing the sensitivity of tumor cells to photothermal treatment. This combination strategy may also allow for lower doses of conventional therapies, minimizing side effects while maximizing therapeutic efficacy.

2.8. In Vivo Biodistribution and Photothermal Effect

Understanding the interaction of GNC and MGL nanoparticles with whole blood or plasma in the bloodstream is essential for assessing their biodistribution behavior in vivo so that they can exert a significant therapeutic effect. Hemocompatibility testing is a key component of the biosafety evaluation of drug carriers, ensuring the safety and efficacy of GNC and MGL by offering critical information on how these carriers interact with blood components. Therefore, to investigate their hemolysis, a series of gradient concentrations were set for the GNC and MGL nanoparticles from low to high concentrations. Figure 3G and Figure S14 (Supporting Information) when the GNC concentration was < 100 $\mu\text{g mL}^{-1}$, the hemolysis rate was < 5%, and when the concentration reached 200 $\mu\text{g mL}^{-1}$, the hemolysis rate was only 7.44%, indicating that the synthesized GNC exhibited good biosafety in vivo, making it a promising nanocore candidate. Additionally, the constructed MGL nanoparticles which were coated with a liposomal layer, further demonstrated enhanced biocompatibility of the material. Even at high concentrations, the hemolysis rate was < 5%, suggesting that these nanoparticles can be safely used in subsequent animal studies.

Based on these promising biological properties, the biodistribution behavior and tumor-targeting capability were further studied using a 4T1 tumor-bearing mouse model. Figure 4A–C shows that free DiR and DiR-labeled MGL demonstrated time-dependent tumor accumulation. More DiR-labeled MGL accumulated in tumor tissues than free DiR, generating a fluorescent signal 3.67-fold higher than that of DiR at 24 h. Free DiR was rapidly metabolized from the liver and had a short in vivo half-life. Within the 36-h detection period, DiR-labeled MGL was observed to exhibit significantly higher fluorescence intensity and greater accumulation in tumor tissues compared to that of the free DiR. Even after 36 h, DiR-labeled MGL accumulation in the tumor lesions remained significantly elevated, ≈ 2.42 times greater than that of free DiR. These findings suggest that the liposomal encapsulation on the surface of the material and PEG₂₀₀₀ modification have a good EPR effect, leading to effective

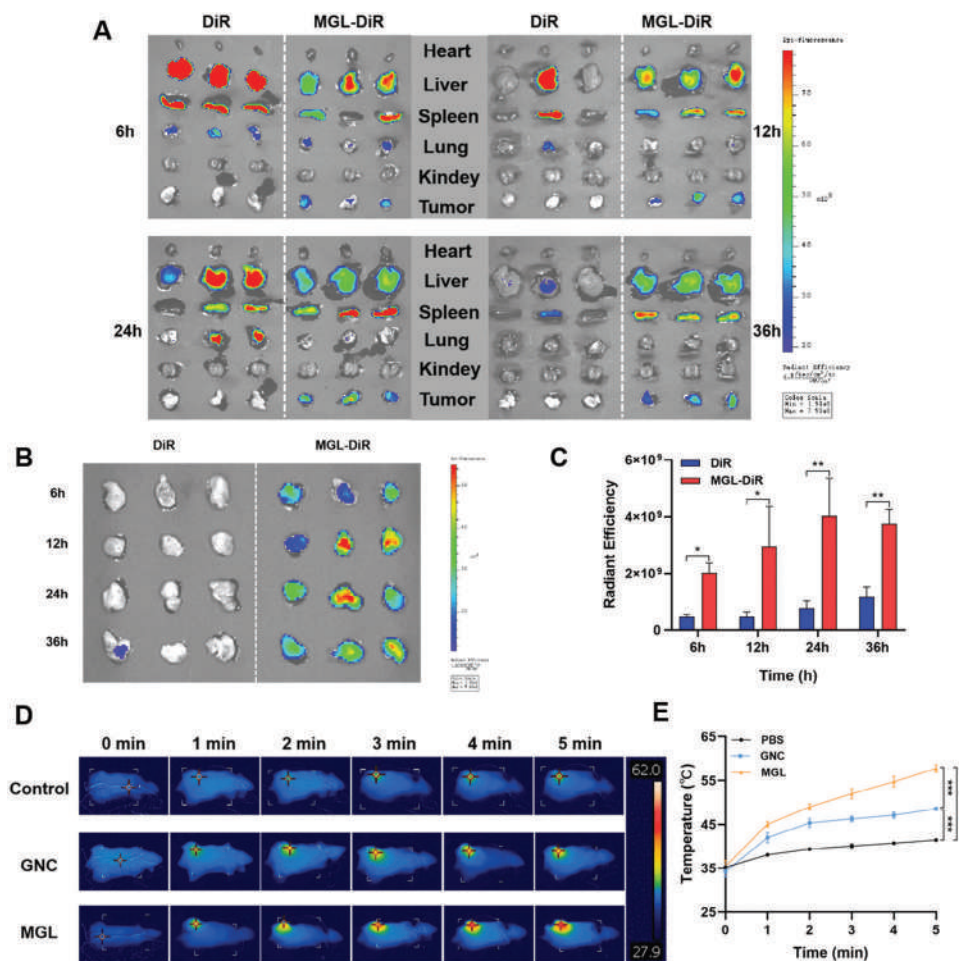


Figure 4. Biodistribution and tumoral temperature study of MGL. A) Representative luminescence images of the major organs (heart, liver, spleen, lung, and kidney) and the tumor upon of 4T1 tumor-bearing mouse post intravenous administration of DiR, and MGL-DiR over different time points. B) Biodistribution patterns and C) Quantification luminescence histogram of DiR and MGL-DiR in tumor of 4T1 tumor-bearing mouse over different time points. D) Photothermal imaging and E) Tumoral temperature analysis of the mice using an IR camera after treatment with PBS, GNC, and MGL. Data are displayed as mean \pm SD ($n = 3$), * $p < 0.05$, ** $p < 0.01$, and *** $p < 0.001$.

accumulation at the tumor site and prolonging the half-life to achieve long in vivo circulation. This enhanced targeting is critical for maximizing therapeutic efficacy while minimizing potential side effects.

Using a near-infrared imaging system, temperature changes in the PBS, GNC, and MGL groups were monitored further to assess the in vivo photothermal efficacy of MGL. Laser treatment and photothermal assessment were performed at the 24-h laser irradiation time point in 4T1 tumor-bearing mice, corresponding to the peak accumulation of the carrier in the tumor. Figure 4D,E shows that after 5 min of laser irradiation, the temperature of the PBS group increased only slightly, whereas the temperature change in the GNC and MGL groups exhibited a significant time-dependent rise. At the same GNC concentration, MGL exhibited a consistently higher temperature at each time point than that of the GNC group. After 5 min of laser irradiation, the temperature rose to >55 °C, meeting the temperature requirement for tumor photothermal treatment. These findings suggest that the prepared MGL nanoparticles exhibit a good photothermal in vivo effect.

2.9. In Vivo Antitumor Efficacy and Immune Activation

In light of the ideal in vitro performance, the synergistic effects of GSH depletion and photothermal immunotherapy mediated by MGL were investigated. GNC, MAL, and MGL were administered intravenously to different groups of 4T1-Luc orthotopic transplanted tumor-bearing mice. When the average bioluminescence intensity reached $\approx 1 \times 10^7$, the mice were randomly assigned to six distinct groups: PBS, GNC, MAL, MGL, GNC with irradiation, and MGL with irradiation ($n = 5$ per group). Following the preliminary studies, all groups underwent three treatment cycles, with bioluminescence intensity at the tumor site monitored utilizing the IVIS small-animal imaging system. In each cycle, intravenous drug administration occurred on the first day, followed by laser irradiation (808 nm, 1.5 W cm^{-2} , 5 min) after a 24-h interval for the photothermal therapy groups. Figure 5A,B shows the bioluminescence images and bioluminescence intensity curve diagram, displaying the bioluminescence intensity of the PBS and GNC groups increased progressively over time, with a faster tumor growth rate in the later stages. These observations

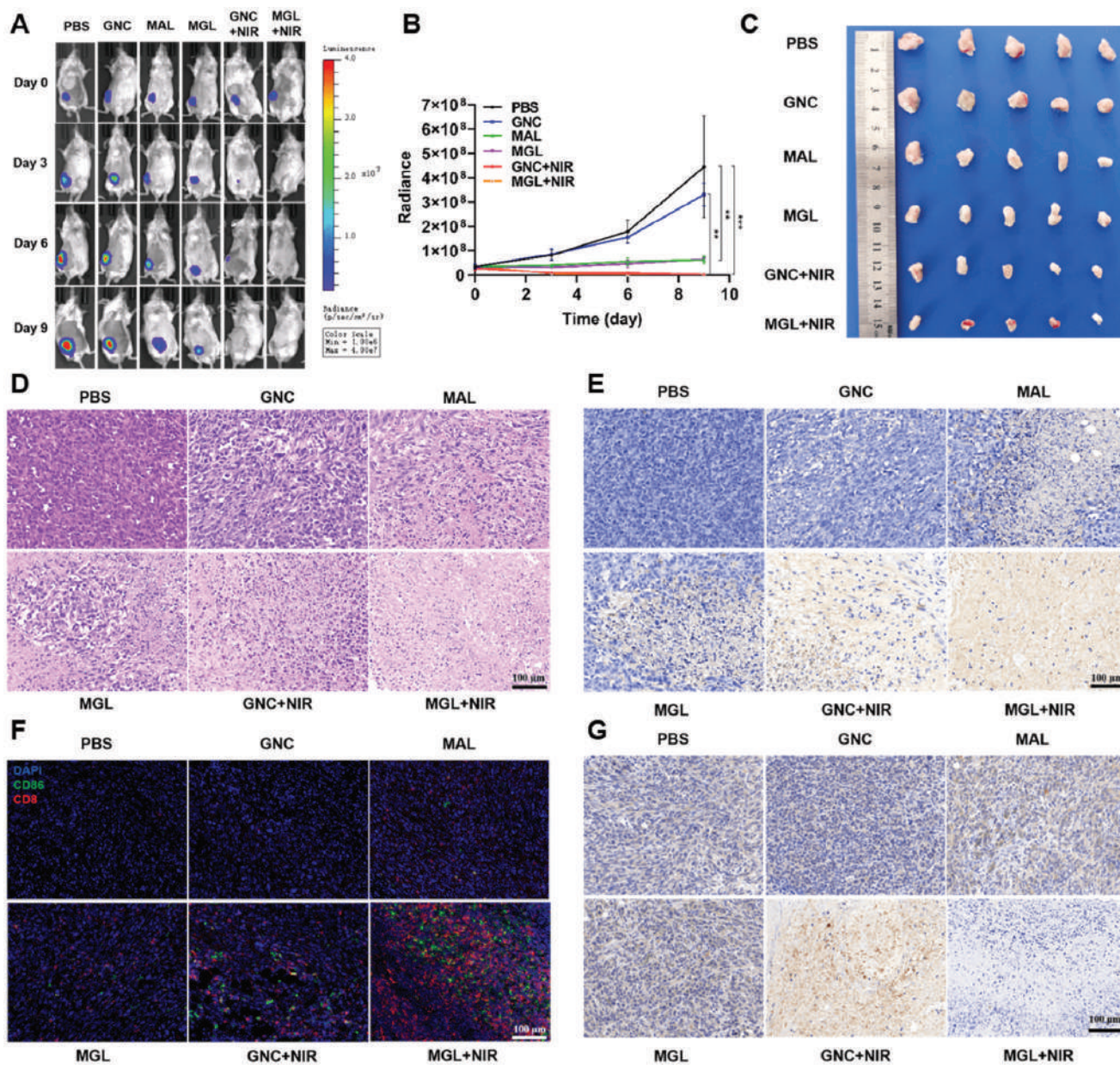


Figure 5. Investigating the comprehensive synergistic therapeutic effect of MAL and MGL in vivo. A) Representative bioluminescence images of the mice were displayed from each treatment group. B) Quantification of bioluminescence intensity of each orthotopic transplantation tumor-bearing mice after treatment with PBS, GNC, MAL, MGL, GNC + NIR, and MGL + NIR. C) Representative photographs of excised 4T1 tumors from mice treated with PBS, GNC, MAL, MGL, GNC + NIR, and MGL + NIR, and tumors were collected for further analysis. D) Representative H&E staining and E) TUNEL staining of tumor slices obtained from tumor-bearing mice treated with various treatments (Scale bar: 100 μ m). F) Representative immunofluorescence (IF) staining images in the tumor section show CD86⁺ macrophages and CD8⁺ T cells infiltration after treatment with various treatments (Scale bar: 100 μ m). G) Representative immunohistochemistry staining images in the tumor section show HSP 70 expression levels after treatment with various treatments (Scale bar: 100 μ m). Data are displayed as mean \pm SD ($n = 5$), * $p < 0.05$, ** $p < 0.01$, and *** $p < 0.001$.

suggest that GNC alone did not affect tumor inhibition. The MAL and MGL treatment groups effectively inhibit tumor cell proliferation, with the bioluminescence intensity not significantly increasing during the three treatment cycles. The GNC with irradiation (photothermal treatment group) and the MGL with irradiation (synergic treatment group) demonstrated significant tumor growth inhibition. The synergic treatment group exhibited the most pronounced therapeutic effect from the first dose, main-

taining a significantly lower bioluminescence intensity than that of the other groups at each time point. After 12 days of treatment, the tumor was excised, revealing that the changing trend in tumor size and weight across the groups was consistent with the changing trend of bioluminescence intensity. The MGL with irradiation group exhibited the most significant effect on tumor size and weight (Figure 5C; Figure S15, Supporting Information), indicating that GNC-mediated photothermal treatment effectively

eradicated tumor cells. Moreover, this antitumor effect can be further enhanced through the synergistic treatment with MAL.

Changes in spleen volume and weight during cancer treatment are clinically significant, as they aid in assessing the immune landscape treatment responses and detecting potential complications early. Therefore, changes in spleen size and weight were monitored. The results showed significant spleen enlargement in the PBS and GNC groups and a decrease in the MAL and MGL groups compared to that in the PBS group. The GNC with irradiation group showed a further reduction in spleen weight, whereas the MGL with irradiation group showed the lowest spleen size, which returned to normal levels (Figure S16, Supporting Information). These results further demonstrated the significant antitumor efficacy of synergistic photothermal immunotherapy. Mouse weights were monitored throughout the treatment cycle, and no significant changes were observed in weight across the different treatment groups after 12 d (Figure S17, Supporting Information). Simultaneously, H&E staining was performed on tissues and organs from mice in each group. Compared to the control (PBS) group, no significant pathological abnormalities were observed in the major organs of each treatment group after treatment, with minimal inflammation or damage observed (Figure 7F). These results further confirm that the constructed MGL nanoparticles had excellent *in vivo* biosafety.

To assess apoptosis in tumor tissues, H&E and TUNEL staining were subsequently employed. The results showed a minimal trend of apoptosis among tumor cells in the PBS and GNC groups, which correlated with the rapid proliferation and high viability of tumor cells. The GNC with irradiation group further showed an improvement in apoptosis level, whereas the MGL with irradiation group exhibited the highest level of apoptosis of the tumor cells (Figure 5D,E). This suggests that the synergistic approach combining photothermal and immunotherapeutic strategies can efficiently kill the cells on the surface or even deep layers of the tumor, achieving optimal antitumor effect.

Considering the sufficient photo-triggered hyperthermia and GSH depletion achieved by MGL at tumor sites, the immune activation in 4T1 tumor-bearing mice in response to the ICD effect was further evaluated. Therefore, immunofluorescence staining was utilized to detect CD86 and CD8 expressions in tumor tissues and verify DC maturation and the activation level of cytotoxic T cells *in vivo*. Among them, green and red fluorescence represent CD86 and CD8 expression levels, respectively. ROS oxidative stress induced by PTT and MAL were observed to promote the CD86 and CD8 expression levels. The MGL with irradiation group had the highest levels of CD86 and CD8 expression (Figure 5F), indicating that the combination treatment can effectively enhance DC maturation. Furthermore, CD8⁺ T cells were activated to enhance the infiltration of cytotoxic T cells into tumor tissues, potentially enhancing the immune response in tumor growth inhibition. To further assess whether the enhanced antitumor immune response *in vivo* could successfully regulate HSP 70 expression in tumor tissues, the HSP 70 expression in different treatment groups was detected using immunohistochemical staining. In this staining, the brown areas represent HSP 70 expression levels. Compared to the PBS and GNC groups, the HSP 70 expression level in the MAL and MGL groups was significantly increased, which may be attributed to the upregulation of ROS levels induced by the depletion of GSH by MAL at the tumor site.

While HSP 70 functions as an intracellular protective protein, it can be used as a protective protein under stress, increasing the expression levels of these genes. Although the GNC with irradiation group can effectively kill tumor cells through photothermal treatment, it also led to an upregulation of HSP 70 expression. Compared to the GNC with irradiation group, the MGL with irradiation group showed significant downregulation of HSP 70 expression, with levels even lower than that observed in the PBS group (Figure 5G). This suggests that the enhanced antitumor immune response achieved through the synergistic treatment can effectively downregulate HSP 70 expressions. The sensitivity of tumor cells to light and heat should be improved to further enhance their therapeutic effects.

2.10. Abscopal Effect and Antimetastasis Effect

A bilateral tumor-bearing mouse model of breast cancer was also constructed to assess if an activated immunoreaction has an antitumor effect on untreated distal tumors and to further explore the underlying mechanisms of immune activation *in vivo*. In this model, the left-side tumor served as the primary tumor, while the right-side was the distal tumor. Following drug administration across different groups, only the primary tumor received laser irradiation. The tumor suppression curve trend of primary and distal tumors showed that the GNC group had no significant inhibitory effect on primary tumors, whereas the GNC with irradiation group effectively inhibited tumor growth following laser irradiation. MAL and MGL exhibited a moderate role in tumor inhibition, whereas MGL with the irradiation group demonstrated the most pronounced antitumor effect, which effectively inhibited tumor growth and achieved complete elimination after the first administration. Moreover, the MGL with irradiation group also effectively inhibited tumor growth of distal tumors compared to that of the other groups. After 12 days, three mice from each group were dissected, and the observed changes in the size and weight of the primary and distal tumors aligned with the trends seen in the tumor suppression curves (Figure 6A–C; Figure S18, Supporting Information). No significant change in body weight throughout the treatment period was observed (Figure S19, Supporting Information). These findings indicate that photothermal therapy effectively kills tumor cells and activates the immune response *in vivo*, as well as enhances the immune effect and induces the systemic antitumor immune response under synergistic MAL therapy. The immune activation from the primary tumor can lead to the recruitment and activation of various immune cells that target distal tumors. Specifically, dendritic cells play a crucial role in processing and presenting tumor antigens to T cells, thereby initiating a systemic immune response. This response can enhance the recognition and destruction of tumor cells at distant sites. This can inhibit the growth of the distal tumor and eliminate the primary tumor, further confirming the potent antitumor efficacy of photothermal and immune synergistic therapy.

Simultaneously, the mechanism of immune *in vivo* activation was further confirmed. First, immunofluorescence staining was used to observe CRT exposure in primary tumors. Figure 6E shows that the PBS and GNC groups did not induce CRT expression, while the MAL and MGL groups showed only a slight

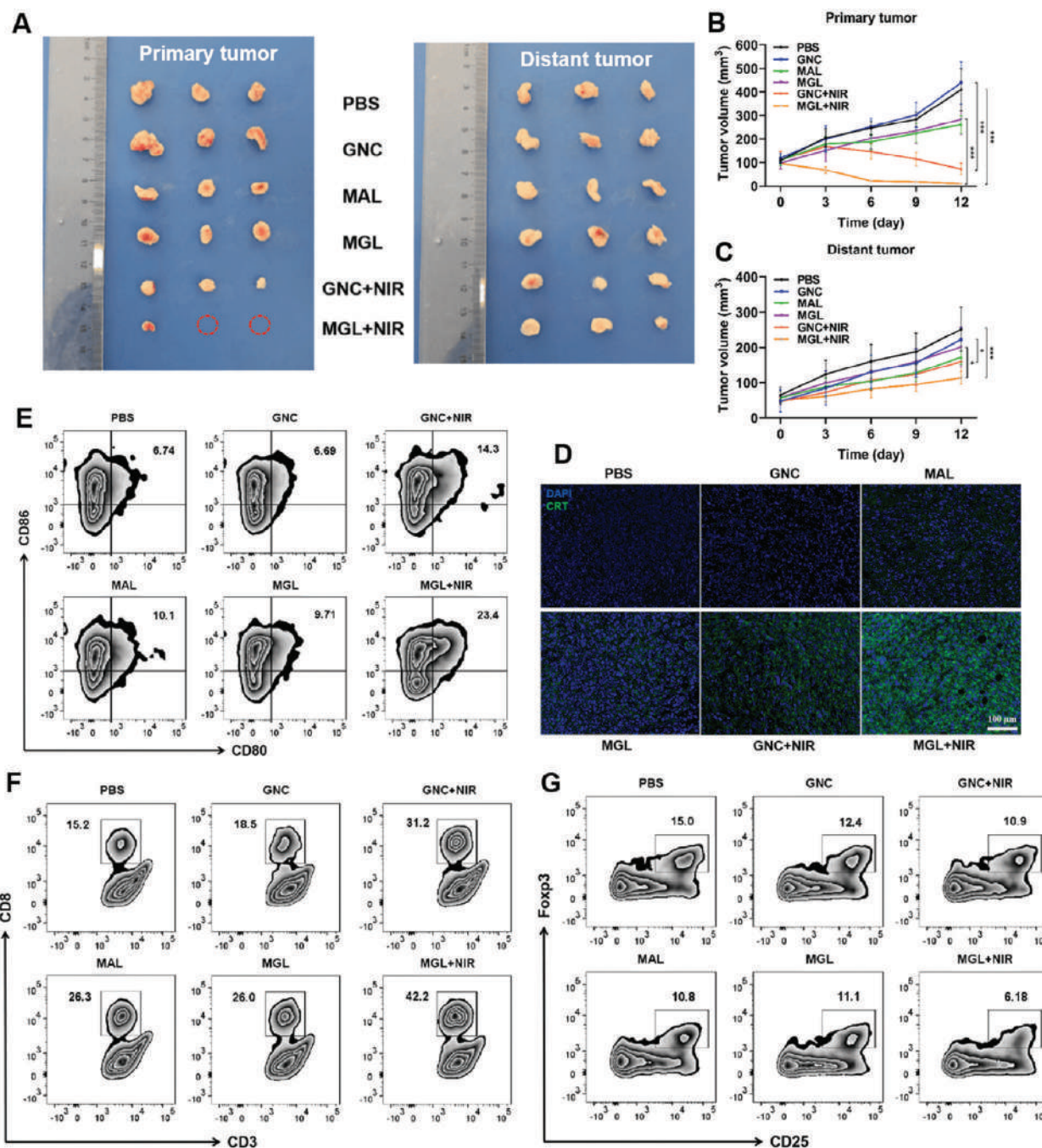


Figure 6. Immune activation and abscopal effect of MGL in vivo. A) Representative photograph of primary tumor and distant tumor of 4T1 tumor-bearing mice over 12 days period post-treatment with PBS, GNC, MAL, MGL, GNC + NIR, and MGL + NIR. B) Primary tumor and C) Distant tumor growth curves of 4T1 tumor-bearing mice over 12 days period post-treatment with PBS, GNC, MAL, MGL, GNC + NIR, and MGL + NIR. D) Representative immunofluorescence (IF) staining images in the tumor section show CRT exposure in primary tumors after treatment with various treatments (Scale bar: 100 μ m). E) The maturation of DC cells, F) activation of CD8⁺ T cells, and G) immunosuppression regulatory T cells (T_{reg}) frequencies in distant tumors after treatment with various treatments.

increase in the CRT-associated green fluorescence. The GNC with irradiation group further enhanced the fluorescence intensity, whereas the MGL with irradiation group showed the strongest green fluorescence intensity, and its CRT expression was much higher than that of the other groups. The results

showed that photothermal therapy successfully induces the ICD effect in vivo and enhances CRT expression. The synergistic MAL further enhanced the ICD effect, thereby releasing DAMPs. These released DAMPs were recognized by pattern recognition receptors on DCs, triggering their activation and enhanced

maturation. Therefore, the proportions of CD80 and CD86 cells in the Shuangyang region were analyzed using flow cytometry to assess DC maturation in distal tumors treated with different materials. Figure 6F and Figure S20 (Supporting Information) show no significant change in the DC maturation rate in the GNC group compared to that of the PBS group (6.74%). However, MAL-induced ROS oxidative stress and photothermal treatment with GNC enhanced DC maturation to a certain extent, whereas the highest DC maturation rate was observed in the MGL with irradiation combined treatment group. This significantly increased to $\approx 23.4\%$. These results suggest that MAL can serve as an immune adjuvant to promote DC maturation, and photothermal therapy can effectively enhance DC maturation and activate the adaptive immune system in vivo.

DCs serve as important antigen-presenting cells, effectively activating and enhancing the differentiation of CD8⁺ T cells following successful antigen presentation. The infiltration of CD8⁺ T cells into distant tumors after treatment with different materials was further analyzed using flow cytometry. Figure 6G and Figure S21 (Supporting Information) show that the change trend was consistent with that of DCs. The MGL+NIR group exhibited the highest proportion of CD8⁺ T cells, significantly increasing to 42.2%, which was significantly higher than that in the GNC with irradiation (31.2%) and MAL (26.3%) groups. The results showed that photothermal therapy effectively activated CD8⁺ T cells, with the MAL immune adjuvant further enhancing the activation and infiltration of cytotoxic T cells within the tumors, thereby successfully triggering the immune response of the body. Subsequently, the immune response was negatively regulated by Treg, with Foxp3 serving as the primary marker for Treg cells. Figure 6H and Figure S22 (Supporting Information) show that the MAL, MGL, and GNC with irradiation groups were observed to effectively reduce Treg cells proportion in tumors compared to that of the PBS group (15%), with the MGL with irradiation group achieving a significant reduction to 6.18%. Additionally, the synergistic therapy significantly upregulated the secretion levels of cytokines such as TNF- α , IFN- γ , and IL-6 in distant tumors (Figure 7A–C), which are key markers of T cell-mediated immune responses and can further confirm the degree of immune response activation. These results confirm that the synergistic treatment combining photothermal therapy and MAL not only effectively enhances the maturation of DCs and the activation and infiltration of CD8⁺ T cells, activates the antitumor immune response, but also reduces the proportion of Treg cells in tumor tissues. This further enhances the immune response, achieving a successful synergistic photothermal and immune therapy.

The immune-mediated antimetastasis effect was studied in a 4T1 lung metastasis model. After the initial treatment, the remaining three mice were injected intravenously with 4T1 cells. One week later, the PBS and GNC groups exhibited a large number of metastatic lesions. Conversely, the MAL and MGL groups showed fewer tumor nodules, and the GNC with irradiation group had only a small number of metastases. In the MGL with irradiation group, metastatic lesions were significantly reduced or completely absent (Figure 7D). H&E staining results showed extensive tumor cell metastasis in the lung tissues of the PBS and GNC groups. Conversely, tumor cell presence was significantly reduced in the MAL, MGL, and GNC with irradiation treatment groups. The MGL with irradiation group showed no detectable

tumor cell metastasis, with the lung tissues returning to normal levels (Figure 7E). The results showed that the systemic antitumor immune response induced by synergistic therapy had an immune memory effect and an excellent antimetastasis effect.

3. Conclusion

In summary, we successfully developed a photo-triggered liposomal gold nanoadjuvant capable of precise hyperthermia and controlled delivery of GSH depletion for remodeling the tumor immune microenvironment and facilitating synergistic photothermal immunotherapy. The thermosensitive liposome shell, with its bilayer membrane structure, offers significant advantages, including controlled drug release, enhanced stability and targeting, and minimized side effects. Photo-triggered MGL enhanced localized hyperthermia, accompanied by thermo-responsive MAL release and GSH depletion, which significantly elevated intracellular ROS levels and enhanced photothermal-induced immunogenic cell death. Furthermore, the activated and expanded DCs and CD8⁺ T lymphocytes at the tumor site enhanced the secretion of various cytokines, such as TNF- α , and reduced intracellular HSP expression, which makes these cells more sensitive to hyperthermia and immunotherapeutic interventions.^[34] Additionally, MGL effectively reprogrammed the immunosuppressive TME by enhancing DC maturation and lymphocyte infiltration within the tumors. Therefore, this process activated a more robust antitumor immune response and established long-term immune memory, significantly inhibiting primary and distal tumors while effectively preventing metastasis to other organs. This light-triggered nanoadjuvant, combined with synergistic GSH depletion and photothermal immunotherapy strategy, is believed to effectively address the inherent limitations of single therapies as well as foster a more robust antitumor immune response. For effectively inhibiting tumor growth, recurrence, and invasion, this synergistic antitumor treatment strategy establishes a theoretical framework laying the groundwork for clinical therapeutic concepts and applications. This offers inspiration for the design of future pharmaceuticals.

4. Experimental Section

Materials: Chlorauric acid trihydrate (HAuCl₄), Maleimide, and dimethyl sulphone were acquired from Aladdin Biochemical Technology Co., Ltd (Shanghai, China). Glycol chitosan was purchased from GlpBio (Californian, USA). Cholesterol was purchased from Avanti (New Jersey, USA). DPPC and DSPC were obtained from AVT Pharmaceutical Technology Co., Ltd. (Shanghai, China). mPEG₂₀₀₀-DSPE was obtained from Ponsure Biotechnology (Shanghai, China). RPMI-1640 and trypsin were obtained from HyClone (Logan, Utah, USA). Phosphate buffered saline (PBS) and fetal bovine serum (FBS) were acquired from Herui Biotechnology (Fujian, China). Fluorescein isothiocyanate (FITC), Reactive oxygen species (ROS) detection kit, reduced glutathione (GSH) assay kit, Annexin V-FITC/PI Apoptosis assay kit, enhanced ATP detection kit were purchased from Biyuntian Biotechnology Co., Ltd (Shanghai, China). CRT and HSP70 antibodies were purchased from Bioss (Beijing, China). Mouse HMGB1, TNF- α , IFN- γ , and IL-6 ELISA kits were obtained from Thermo Fisher Scientific (Waltham, MA, USA). All other chemical reagents were obtained from Sinopharm Chemical Reagent Corporation (Shanghai, China).

Cell Lines and Animal Studies: Murine breast cancer cell lines 4T1 and EMT-6 were acquired from MeisenCTCC Cell Technology Co., Ltd (Zhejiang, China) and were cultured in RPMI-1640 supplemented with

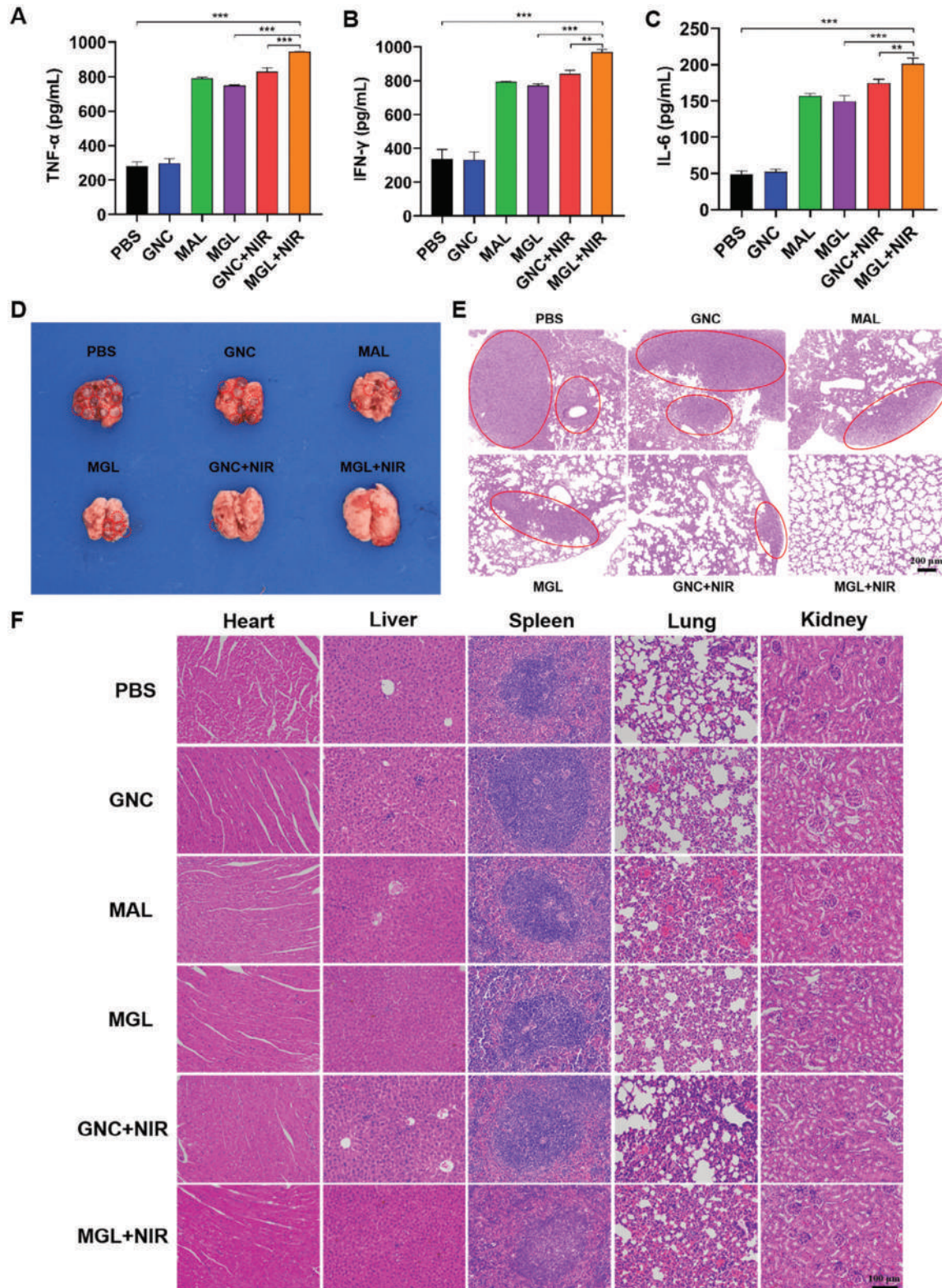


Figure 7. Anti-metastasis effect of MGL in vivo. A) Contents of tumor necrosis factor- α (TNF- α), B) interferon- γ (IFN- γ), and C) interleukin-6 (IL-6) in distant tumors after treatment with PBS, GNC, MAL, MGL, GNC + NIR, and MGL + NIR. D) Representative photographs and E) H&E staining of lung tissues with tumor metastasis after treatment with various treatments (Scale bar: 100 μ m). F) Representative H&E images of the tissues including heart, liver, spleen, lung, and kidney from 4T1 xenograft-bearing mice after intravenous administration of PBS, GNC, MAL, MGL, GNC + NIR, and MGL + NIR (Scale bar: 100 μ m).

penicillin/streptomycin (1%, w/v) and 10% FBS. All cells were cultured in a humidified atmosphere containing 5% CO₂ at a temperature of 37 °C.

BALB/c mice (female, 18–22 g) were acquired from SLAC Laboratory Animal Co., Ltd (Shanghai, China) and housed under specific pathogen-free (SPF) conditions in a controlled environment. All animals were kept in standard laboratory cages with a 12-h light/dark cycle and maintained at a constant temperature (22 ± 3 °C) and humidity (50 ± 10%). They had access to sterilized rodent chow and filtered water ad libitum. Regular monitoring ensured their health and well-being throughout the study. All animal experiments were performed in compliance with the Guidelines for the Care and Use Ethics Committee of Fujian Medical University (Certificate number: FJMU IACUC 2021-0463).

Preparation of MGL—Synthesis of GNC: Ethylene glycol (30 mL) was heated and stirred in a round-bottom flask at 170 °C for 1 h, and glycol solutions of Na₂S (0.72 mg mL⁻¹, 400 μL), PVP (20 mg mL⁻¹, 7.5 mL) and AgNO₃ (48 mg mL⁻¹, 2.5 mL) were added successively. After the reaction continued for 10 min, AgNCs solution was obtained by centrifuge washing with acetone and deionized water for 3 times. Then take 500 μL AgNCs solution, add PVP (1 mg mL⁻¹, 5 mL) aqueous solution, stir, and react at 100 °C for 10 min, and then add 0.5 mM HAuCl₄ solution drop by drop to stop the reaction when the maximum absorption wavelength is close to 800 nm. GNC solution was obtained by centrifuge washing with NaCl-saturated solution and deionized water for 3 times.

Preparation of MGL: Gold nanocage solution with 900 μg GNC equivalent, maleimide (10 mg mL⁻¹, 1 mL), and glycol chitosan (2 mg mL⁻¹, 1 mL) solution were stirred at room temperature for 4 h to obtain MAL@GNC solution for use. Then, 6.5 mg DPPC, 1 mg DSPC, 1.78 mg mPEG2000-DSPE, and 0.74 mg cholesterol were used to prepare lipid films, and the previously prepared MAL@GNC solution was dispersed by thin film to prepare MGL nanoparticles.

Characterization of MGL: The mean hydrodynamic diameter, polydispersity index (PDI), and zeta potential of the GNC and MGL were analyzed DLS (Anton Paar, USA). The silver and gold content of AgNCs, GNC, and MGL were detected by ICP-OES (Perkin Elmer, USA). The UV-Vis absorption spectra of MGL were recorded in the range 300–100 nm using a UV-2600 spectrophotometer (Shimadzu, Japan). The MAL content in the MGL was detected by HPLC (Agilent, USA), which was equipped with a ChromCore C18 column (150 × 4.6 mm, 5 μm; Welch Materials, Inc., Ellicott, MD, USA). The morphologies of the AgNCs, GNC, and MGL were characterized by TEM (Thermo Fisher, USA).

Dissolve GSH in PBS (pH 7.4) and react with free MAL at different molar ratios at 37 °C for 4 h, then measure the unreacted glutathione content by the Ellman method to indirectly assess MAL-mediated GSH depletion capacity.

The particle size change trend of MGL solution stored at 4 °C and PBS (pH 7.4) within 7 days was analyzed by DLS, and 50 μL MGL was diluted to 1 mL with PBS each time for detection.

Photothermal Efficiency Analysis of MGL: To assess the temperature changes caused by GNC and MGL at different concentrations (C_{Au} = 5, 8, 10, and 20 μg mL⁻¹), which were exposure to NIR laser irradiation for 5 min at a power density of 1.5 W cm⁻², with temperature changes of the dispersions were recorded every 0.5 min. To assess the temperature changes caused by GNC and MGL by different laser power, 200 μL GNC and MGL solutions (C_{Au} = 10 μg mL⁻¹) were exposure to NIR laser irradiation (0.5, 1, and 1.5 W cm⁻²), with temperature changes of the dispersions were recorded every 0.5 min. To assess the photothermal stability, 200 μL MGL solution (C_{Au} = 8 μg mL⁻¹) was removed to the 96-well plate, the laser power was set to 1.5 W cm⁻², and then the temperature probe was placed into the solution every 30 s to detect the change of the solution temperature over time. After 7 min, the illumination was stopped and the temperature was cooled down for 7 min. Continue to light, cycle measurement 3 times.

Cellular Internalization and Intracellular GSH Detection of MGL: The Cellular internalization of MGL was evaluated on 4T1 and EMT-6 cells. To track the MGL, FITC was encapsulated into liposome to obtain FITC-loaded MGL. Logarithmic growth stage cells were uniformly inoculated into 8-cavity pores, and the cells were treated with FITC-loaded MGL for 0.5, 1, 2, and 4 h, respectively. Then nuclear staining was performed with

DAPI, and the trend of FITC fluorescence intensity was observed under a confocal laser microscope. MGL uptake by cells was evaluated by FACS. 4T1 and EMT-6 cells of the logarithmic growth stage were uniformly inoculated into 6-well plates, and the cells were treated with FITC-loaded MGL for 0.5, 1, 2, and 4 h, respectively. Then the cells were digested, and the fluorescence intensity of FITC in cells was quantitatively analyzed by flow cytometry.

4T1 and EMT-6 cells were treated with MAL and MGL (2 μg mL⁻¹ MAL equivalent) for 6 h, respectively, and then GSH levels were detected with a reduced glutathione (GSH) assay kit. Intracellular ROS levels were detected using DCFH-DA as a fluorescent probe. 4T1 and EMT-6 cells were treated with MAL and MGL (2 μg mL⁻¹ MAL equivalent) for 6 h, respectively, and then stained with DCFH-DA for 30 min. After washing with PBS twice, the fluorescence intensity of ROS was observed under CLSM.

Cytotoxicity Analysis and Migration Inhibition of MGL: The cytotoxicity of different treatment groups on 4T1 and EMT-6 cells was measured by the MTT method. The density of 4000 cells per well of 4T1 and EMT-6 cells were inoculated into 96-well plates, and then the groups containing NIR were exposed to light (808 nm, 1.5 W cm⁻², 5 min) after incubation with different concentrations of GNC, MAL, and MGL for 4 h. And continue to culture until 24 h. The prepared MTT solution (100 μL, 50 μg mL⁻¹) was added to each well and cultured for 4 h. The cell medium was replaced with DMSO (150 μL). The absorbance of each well was recorded at 490 nm wavelength and standard MTT analysis was performed. The effects of different treatment groups on apoptosis levels of 4T1 and EMT-6 cells were analyzed by flow cytometry. The density of 2 × 10⁵ cells per well of 4T1 and EMT-6 cells was inoculated into 12-well plates, respectively. After incubation with GNC, MAL, and MGL (1 μg mL⁻¹ MAL or 8 μg mL⁻¹ GNC equivalent) for 4 h, the group containing NIR was exposed to light (808 nm, 1.5 W cm⁻², 5 min) and continued to culture for 24 h. The cells and their supernatant were collected, and stained with Annexin V-FITC and PI for 20 min, respectively, and the apoptosis level was detected by flow cytometry. The migration and repair ability of 4T1 and EMT-6 cells under different treatment groups were observed by cell scratch experiment. The density of 3 × 10⁵ cells per well of 4T1 and EMT-6 cells were inoculated into 6-well plates, respectively, and scratch photos were taken at 0 h under an inverted fluorescence microscope. Then, after incubation with GNC, MAL, and MGL (1 μg mL⁻¹ MAL or 8 μg mL⁻¹ GNC equivalent) for 4 h, the group containing NIR was exposed to light (808 nm, 1.5 W cm⁻², 5 min) and continued to culture for 24 and 24 h scratches were photographed for analysis of cell migration.

ICD Inducing Capability: For the detection of CRT expression level, 4T1 and EMT-6 cells of the logarithmic growth stage were uniformly inoculated into 8-chamber pores, respectively. After incubation with GNC, MAL, and MGL (1 μg mL⁻¹ MAL or 8 μg mL⁻¹ GNC equivalent) for 4 h, the group containing NIR was subjected to irradiation (808 nm, 1.5 W cm⁻², 5 min) and continued culture until 24 h. The cells were fixed with 4% paraformaldehyde for 10 min, and then incubated with CRT antibody against light for 1.5 h. Finally, the cell nucleus was stained with DAPI, and the trend of CRT fluorescence intensity was observed under CLSM. For the detection of HMGB1 secretion level, the density of 2 × 10⁵ cells per well of 4T1 and EMT-6 cells per well was inoculated into 12-well plates, and then GNC, MAL, and MGL (1 μg mL⁻¹ MAL or 8 μg mL⁻¹ GNC equivalent) were administered and incubated for 4 h. The group containing NIR was exposed to light (808 nm, 1.5 W cm⁻², 5 min) and continued to culture for 2 h. The supernatant of each well was detected by an ELISA kit. For the detection of ATP, the supernatant of 4T1 and EMT-6 cells treated in different groups was collected for the detection of ATP kit.

MGL Reprograms the TME and Inhibits HSP Expression: The density of 3 × 10⁵ cells per well of 4T1 and EMT-6 cells per well was inoculated into 6-well plates, and then GNC, MAL, and MGL (1 μg mL⁻¹ MAL or 8 μg mL⁻¹ GNC equivalent) were used for incubation for 4 h, and the group containing NIR was subjected to irradiation (808 nm, 1.5 W cm⁻², 5 min). In the TNF-α group, MGL+NIR was supplemented with 20 ng TNF-α for intervention, and the culture was continued until 24 h. The cell protein was extracted for Western Blot analysis.

In Vivo Biodistribution and Photothermal Effect: The mice were sacrificed and main tissues (including the tumors, liver, heart, spleens, lungs,

and kidneys) were harvested at 60, 180, 360, 540, and 720 min ($n = 3$), and thoroughly rinsed in ice-cold PBS to remove the superficial blood and other debris, and then stored at -80°C until analysis.

The collected tissue samples were weighed, diced into small pieces, and homogenized in three volumes of ice-cold PBS. Subsequently, 100 μL tissue homogenate was spiked with 10 μL epirubicin (internal standard working solution), mixed by vortexing with 300 μL methanol for 10 min, and centrifuged at $15000 \times g$ for 15 min at 4°C to precipitate proteins. The resultant supernatants (5 μL) were measured using HPLC–MS/MS.

Different concentrations of GNC and MGL were added to 4% (v/v) erythrocyte suspension, mixed, incubated at 37°C for 30 min, and centrifuged to obtain the supernatant. Then the absorbance of each supernatant at 545 nm wavelength was measured by ultraviolet spectrophotometry, and the hemolysis rate was calculated.

To evaluate the biodistribution and tumor targeting of MGL, an orthotopic tumor model was established using BALB/c mice (female, 18–22 g) and 4T1-Luc cells. When the tumor volume reached $\approx 200 \text{ mm}^3$, the mice were randomly divided into DiR, and DiR-loaded MGL groups and the specified formulations were administered intravenously through the tail vein. The mice were sacrificed and main tissues (including the heart, liver, spleen, lung, kidney, and tumor tissues) were harvested at 6, 12, 24, and 36 h ($n = 3$), and thoroughly rinsed in ice-cold PBS to remove the superficial blood and other debris, and then stored at -80°C until analysis.

The in vivo photothermal effect of MGL was evaluated on the 4T1 orthotopic tumor model, and three groups of Control, GNC, and MGL were set up. After 24 h of caudal vein administration, mice were anesthetized with 2% pentobarbital sodium solution and subjected to near-infrared laser irradiation (808 nm, 1.5 W cm^{-2} , 5 min), and temperature changes at the tumor site were monitored by thermal imager.

In Vivo Antitumor Efficacy and Immune Activation: Female BALB/c mice bearing 4T1 tumors in an orthotopic were randomly assigned to six groups as follows: PBS, GNC, MAL, MGL, GNC with irradiation, and MGL with irradiation ($n = 5$). When the tumor bioluminescence intensity reached more than 1×10^7 , the mice were administered different treatments. After 24 h of caudal vein administration, the group containing NIR was irradiated by laser (808 nm, 1.5 W cm^{-2} , 5 min), and the bioluminescence intensity of the mice was monitored at 3, 6, and 9 days after administration, and the weight was weighed and the weight change was recorded. After 12 days of observation, the mice were euthanized and their heart, liver, spleen, lung, kidney, and tumor tissues were taken to measure the size change trend of tumor and spleen in different groups, and the tumors in different treatment groups were analyzed by H&E, TUNEL, immunohistochemistry, and immunofluorescence staining.

4T1 cells were injected subcutaneously into the back of mice on the left (8×10^5 cells) and the right (4×10^5 cells), which were called primary and distal tumors, respectively. When the primary tumor volume reached $\approx 100 \text{ mm}^3$ and the distal tumor volume reached 50 mm^3 , the tumor-bearing mice were randomly assigned to 6 groups ($n = 5$), namely PBS (control group), GNC, MAL, MGL, GNC with irradiation and MGL with irradiation groups. After 24 h of caudal vein administration, the group containing NIR was irradiated by laser (808 nm, 1.5 W cm^{-2} , 5 min), and the tumor volume and weight changes of each group were measured at 3, 6, 9, and 12 days after administration, respectively. After 12 days of observation, 3 mice in each group were euthanized, the primary and distal tumors were collected, photographed, weighed, and used for follow-up immunological analysis.

Abscopal Effect and Antimetastasis Effect: On the 7th day after administration, the primary tumors of mice were collected for CRT immunofluorescence staining, and the CRT expression in different treatment groups was analyzed. DC maturation and T cell infiltration levels in the distal tumor were analyzed by flow cytometry. The tumor was digested and single-cell suspension was collected. In order to study T cell infiltration in distal tumors, antibodies CD45, CD11c, CD80, and CD86 were added to the single-cell suspension of the tumor and incubated at 4°C for 30 min without light. In order to study the maturation of dendritic cells, antibodies CD45, CD3, CD8, CD4, CD25, and Foxp3 were added to the single-cell suspension of the tumor and incubated at 4°C for 30 min without light, and then flow cytometry was performed. Cytokine levels of TNF- α , IFN- γ , and IL-6 in distal tumors were measured by ELISA kit.

The remaining 3 mice in different groups after treatment were injected with 4T1 cells (5×10^5 cells) in the tail vein to construct lung metastasis model. A week later, the lung tissues of mice in each group were photographed and H&E staining was performed to observe the lung metastasis and immune memory effect of different treatment groups.

Statistics Analysis: All experiments were conducted at least three times, and results were presented as mean \pm standard deviation (SD). Statistical analysis and graphing were performed using GraphPad Prism 6 Software (San Diego, USA). A two-tailed Student's t-test was used for all statistical analyses, with significance levels indicated as follows: * $p < 0.05$, ** $p < 0.01$, and *** $p < 0.001$.

Ethics Approval and Consent to Participate: All the animal experiments were approved by the Experimental Animal Center of Fujian Medical University. Animal experiments were carried out in compliance with the Guide for the Animals Care and Ethics Committee of Fujian Medical University (Certificate number: FJMU IACUC 2021-0463).

Supporting Information

Supporting Information is available from the Wiley Online Library or from the author.

Acknowledgements

J.L., K.Z., and L.L. contributed equally to this work. This work was supported by the Major State Basic Research Development Program of China (2023YFB3810000), the National Natural Science Foundation of China (81925019, 22074017, and U22A20333), the National Natural Science Foundation of Fujian Province (2024J01133988). Open Research Fund of Digital Medicine Valley (2024B013). The authors extend their gratitude to Mr. He from Shiyanjia Lab (www.shiyanjia.com) for providing invaluable assistance with the TEM analysis. The authors acknowledge the Fujian Medical University Ethics Committee for their kind guidance in the animal experiments and the Public Technology Service Center of Fujian Medical University.

Conflict of Interest

The authors declare no conflict of interest.

Data Availability Statement

The data that support the findings of this study are available from the corresponding author upon reasonable request.

Keywords

anti-metastatic, gold nanocages, GSH depletion, immunotherapy, photothermal therapy

Received: August 22, 2024
Revised: September 22, 2024
Published online:

- [1] a) X. Yang, C. Yang, S. Zhang, H. Geng, A. X. Zhu, R. Bernards, W. Qin, J. Fan, C. Wang, Q. Gao, *Cancer Cell* **2024**, *42*, 180; b) E. Blass, P. A. Ott, *Nat. Rev. Clin. Oncol.* **2021**, *18*, 215.
- [2] a) P. Zhu, S. Y. Li, J. Ding, Z. Fei, S. N. Sun, Z. H. Zheng, D. Wei, J. Jiang, J. L. Miao, S. Z. Li, X. Luo, K. Zhang, B. Wang, K. Zhang, S. Pu,

- Q. T. Wang, X. Y. Zhang, G. L. Wen, J. O. Liu, J. T. August, H. Bian, Z. N. Chen, Y. W. He, *J. Pharm. Anal.* **2023**, *13*, 616; b) A. Daei Sorkhabi, L. Mohamed Khosroshahi, A. Sarkesh, A. Mardi, A. Aghebati-Maleki, L. Aghebati-Maleki, B. Baradaran, *Front. Immunol.* **2023**, *14*, 1113882.
- [3] Z. Tian, M. Liu, Y. Zhang, X. Wang, *J. Hematol. Oncol.* **2021**, *14*, 75.
- [4] a) T. Fu, L. J. Dai, S. Y. Wu, Y. Xiao, D. Ma, Y. Z. Jiang, Z. M. Shao, *J. Hematol. Oncol.* **2021**, *14*, 98. b) J. Guo, M. Wang, Y. Zhu, F. Watari, Y. Xu, X. Chen, *Acta. Mater. Med.* **2023**, *2*, 172.
- [5] M. Chen, D. Liu, F. Liu, Y. Wu, X. Peng, F. Song, *J. Control. Release.* **2021**, *332*, 269.
- [6] Y. Xiong, C. Xiao, Z. Li, X. Yang, *Chem. Soc. Rev.* **2021**, *50*, 6013.
- [7] a) M. Wang, M. Chang, C. Li, Q. Chen, Z. Hou, B. Xing, J. Lin, *Adv. Mater.* **2022**, *34*, 2106010; b) X. Y. Zhong, X. W. Wang, L. Cheng, Y. A. Tang, G. T. Zhan, F. Gong, R. Zhang, J. Hu, Z. Liu, X. L. Yang, *Adv. Funct. Mater.* **2020**, *30*, 1907954.
- [8] L. Dong, X. Deng, Y. Li, X. Zhu, M. Shu, J. Chen, H. Luo, K. An, M. Cheng, P. Zhang, W. Tan, *J. Am. Chem. Soc.* **2024**, *146*, 19218.
- [9] Y. Liu, X. Wang, H. Feng, X. Li, R. Yang, M. Zhang, Y. Du, R. Liu, M. Luo, Z. Li, B. Liu, J. Wang, W. Wang, F. An, F. Niu, P. He, *J. Nanobiotechnol.* **2024**, *22*, 299.
- [10] Z. Zhou, H. Wu, R. Yang, A. Xu, Q. Zhang, J. Dong, C. Qian, M. Sun, *Sci. Adv.* **2020**, *6*, eabc4373.
- [11] J. Wang, Q. Q. Zhang, Y. C. Li, X. Y. Pan, Y. Y. Shan, J. Zhang, *Chin. Chem. Lett.* **2024**, *35*, 108746.
- [12] a) Y. Yang, Y. Yu, H. Chen, X. Meng, W. Ma, M. Yu, Z. Li, C. Li, H. Liu, X. Zhang, H. Xiao, Z. Yu, *ACS Nano* **2020**, *14*, 13536; b) X. Cheng, H. D. Xu, H. H. Ran, G. Liang, F. G. Wu, *ACS Nano* **2021**, *15*, 8039.
- [13] Y. Lee, S. Song, S. Yang, J. Kim, Y. Moon, N. Shim, H. Y. Yoon, S. Kim, M. K. Shim, K. Kim, *Acta. Pharm. Sin. B* **2024**, *14*, 1428.
- [14] S. Dong, Y. Dong, T. Jia, S. Liu, J. Liu, D. Yang, F. He, S. Gai, P. Yang, J. Lin, *Adv. Mater.* **2020**, *32*, 2002439.
- [15] Z. Sun, G. Deng, X. Peng, X. Xu, L. Liu, J. Peng, Y. Ma, P. Zhang, A. Wen, Y. Wang, Z. Yang, P. Gong, W. Jiang, L. Cai, *Biomaterials* **2021**, *279*, 121228.
- [16] Z. Zhou, H. Liang, R. Yang, Y. Yang, J. Dong, Y. Di, M. Sun, *Angew. Chem., Int. Ed.* **2022**, *61*, 202202843.
- [17] N. Gong, X. Ma, X. Ye, Q. Zhou, X. Chen, X. Tan, S. Yao, S. Huo, T. Zhang, S. Chen, X. Teng, X. Hu, J. Yu, Y. Gan, H. Jiang, J. Li, X. J. Liang, *Nat. Nanotechnol.* **2019**, *14*, 379.
- [18] Q. Chen, C. Liang, X. Sun, J. Chen, Z. Yang, H. Zhao, L. Feng, Z. Liu, *Proc. Natl. Acad. Sci. USA* **2017**, *114*, 5343.
- [19] Z. Wang, N. Yang, Y. Hou, Y. Li, C. Yin, E. Yang, H. Cao, G. Hu, J. Xue, J. Yang, Z. Liao, W. Wang, D. Sun, C. Fan, L. Zheng, *Adv. Sci.* **2023**, *10*, 2302123.
- [20] L. Wang, Y. T. Xu, C. Liu, W. L. Si, W. J. Wang, Y. W. Zhang, L. P. Zhong, X. C. Dong, Y. X. Zhao, *Chem. Eng. J.* **2022**, *438*, 135567.
- [21] a) R. Venkatesan, H. Xiong, Y. J. Yao, J. R. Nakkala, T. Zhou, S. F. Li, C. Y. Fan, C. Y. Gao, *Chem. Eng. J.* **2022**, *446*, 136868; b) B. Merchant, *Biologicals* **1998**, *26*, 49.
- [22] a) L. Yao, D. Bojic, M. Liu, *J. Pharm. Anal.* **2023**, *13*, 960; b) B. Q. Chen, Y. Zhao, Y. Zhang, Y. J. Pan, H. Y. Xia, R. K. Kankala, S. B. Wang, G. Liu, A. Z. Chen, *Bioact. Mater.* **2023**, *21*, 1.
- [23] a) X. Chai, Y. Gu, L. Lv, C. Chen, F. Feng, Y. Cao, Y. Liu, Z. Zhu, Z. Hong, Y. Chai, X. Chen, *J. Pharm. Anal.* **2022**, *12*, 725; b) B. Chen, X. Wang, D. Lin, D. Xu, S. Li, J. Huang, S. Weng, Z. Lin, Y. Zheng, H. Yao, X. Lin, *Int. J. Nanomed.* **2019**, *14*, 6691; c) B. Feng, X. Lu, G. Zhang, L. Zhao, D. Mei, *Acta. Mater. Med.* **2023**, *2*, 216.
- [24] a) D. V. Krysko, A. D. Garg, A. Kaczmarek, O. Krysko, P. Agostinis, P. Vandenabeele, *Nat. Rev. Cancer.* **2012**, *12*, 860; b) C. Li, P. Jiang, S. Wei, X. Xu, J. Wang, *Mol. Cancer* **2020**, *19*, 116.
- [25] B. Chen, K. Zheng, S. Fang, K. Huang, C. Chu, J. Zhuang, J. Lin, S. Li, H. Yao, A. Liu, G. Liu, J. Lin, X. Lin, *J. Nanobiotechnol.* **2023**, *21*, 378.
- [26] Q. Lin, Y. Jing, C. Yan, X. Chen, Q. Zhang, X. Lin, Y. Xu, B. Chen, *Int. J. Nanomed.* **2024**, *19*, 5381.
- [27] W. J. Wang, X. Y. He, X. J. Wang, T. T. Zhao, O. Muraoka, G. Tanabe, W. J. Xie, T. J. Zhou, L. Xing, Q. R. Jin, H. L. Jiang, *Chin. Chem. Lett.* **2024**, *35*, 108656.
- [28] B. Renoux, F. Raes, T. Legigan, E. Péraudeau, B. Eddhif, P. Pointot, I. Tranoy-Opalinski, J. Alsarraf, O. Koniev, S. Kolodych, S. Lerondel, A. Le Pape, J. Clarhaut, S. Papot, *Chem. Sci.* **2017**, *8*, 3427.
- [29] A. Paściak, R. Marin, L. Abiven, A. Pilch-Wróbel, M. Misiak, W. Xu, K. Prorok, O. Bezkravnyy, Ł. Marciniak, C. Chanéac, F. Gazeau, R. Bazzi, S. Roux, B. Viana, V. P. Lehto, D. Jaque, A. Bednarkiewicz, *ACS Appl. Mater. Interfaces.* **2022**, *14*, 33555.
- [30] Y. Chao, C. Liang, H. Tao, Y. Du, D. Wu, Z. Dong, Q. Jin, G. Chen, J. Xu, Z. Xiao, Q. Chen, C. Wang, J. Chen, Z. Liu, *Sci. Adv.* **2020**, *6*, eaz4204.
- [31] L. Li, W. You, X. Wang, Y. Zou, H. Yao, H. Lan, X. Lin, Q. Zhang, B. Chen, *Phytomedicine* **2023**, *108*, 154508.
- [32] L. Ke, F. Wei, L. Xie, J. Karges, Y. Chen, L. Ji, H. Chao, *Angew. Chem., Int. Ed.* **2022**, *61*, 202205429.
- [33] a) J. D. Martin, H. Cabral, T. Stylianopoulos, R. K. Jain, *Nat. Rev. Clin. Oncol.* **2020**, *17*, 251; b) M. Mu, X. Liang, N. Zhao, D. Chuan, B. Chen, S. Zhao, G. Wang, R. Fan, B. Zou, B. Han, G. Guo, *J. Pharm. Anal.* **2023**, *13*, 99.
- [34] Y. Bo, H. Wang, *Adv. Mater.* **2023**, <https://doi.org/10.1002/adma.202210452>.